

## RESEARCH ARTICLE

WILEY

# Multi-channel helical-antenna inner-volume RF coils for ultra-high field MR scanners

Pranav S. Athalve<sup>1</sup> | Milan M. Ilić<sup>1,2</sup> | Pierre-Francois van de Moortele<sup>3</sup> |  
Andrew J. M. Kiruluta<sup>4</sup> | Branislav M. Notaroš<sup>1</sup>

<sup>1</sup>Department of Electrical and Computer Engineering, Colorado State University, Fort Collins, Colorado

<sup>2</sup>School of Electrical Engineering, University of Belgrade, Belgrade, Serbia

<sup>3</sup>Department of Radiology, Center for Magnetic Resonance Research, University of Minnesota, Minneapolis, Minnesota

<sup>4</sup>Radiology Department, Massachusetts General Hospital, Harvard Medical School, Boston, Massachusetts

**Correspondence**

Branislav M. Notaroš, Department of Electrical and Computer Engineering, Colorado State University, Fort Collins, CO. Email: notaros@colostate.edu

**Funding information**

National Science Foundation, Grant/Award Numbers: ECCS-1307863 and ECCS-1810492, Serbian Ministry of Education, Science, and Technological Development, Grant/Award Number: TR-32005

**Abstract**

RF coil design for human ultra-high field (7 T and higher) magnetic resonance (MR) imaging is an area of intense development, to overcome difficult challenges such as RF excitation spatial heterogeneity and low RF transfer efficiency into the spin system. This article proposes a novel category of multi-channel RF volume coil structures at both 7 T and 10.5 T based on a subject-loaded multifilar helical-antenna RF coil that aims at addressing these problems. In some prior applications of helix antennas as MR RF coils at 7 T, the imaged sample was positioned outside the helix. Here, we introduce a radically different approach, with the inner volume of a helix antenna being utilized to image a sample. The new coil uniquely combines traveling-wave behavior through the overall antenna wire structure and near-field RF interaction between the conducting elements and the imaged tissues. It thus benefits from the congruence of far- and near-field regimes. Design and analysis of the novel inner-volume coils are performed by numerical simulations using multiple computational electromagnetics techniques. The fabricated coil prototypes are tested, validated, and evaluated experimentally in 7-T and 10.5-T MR human wide bore (90-cm) MR scanners. Phantom data at 7 T show good consistency between numerical simulations and experimental results. Simulated  $B_1^+$  transmit efficiencies, in  $T/\sqrt{W}$ , are comparable to those of some of the conventional and state-of-the-art RF coil designs at 7 T. Experimental results at 10.5 T show the scalability of the helix coil design.

**KEYWORDS**

10.5-T MR scanner, 7-T MR scanner,  $B_1^+$  transmit efficiency, multi-channel helical-antenna inner-volume RF coils, RF volume coils, ultra-high field MRI

## 1 | INTRODUCTION

Ultra-high field (UHF), high field, and low field magnetic resonance (MR) scanners are usually referring to the main polarizing static magnetic field values of  $B_0 \geq 7$  T (ie, Larmor frequency  $f_0 \geq 300$  MHz),  $3 \text{ T} \leq B_0 < 7 \text{ T}$ , and  $B_0 < 3 \text{ T}$ , respectively. Whereas most clinical scanners operate at either 1.5 T or 3 T, cutting-edge research centers in neuroscience and/or MR imaging (MRI) tend to favor UHF-MR scanners

because the higher signal-to-noise ratio (SNR) at the UHF  $B_0$  field strength can be traded for higher spatial resolution (hundreds of microns), as well as higher parallel imaging performances allowing for higher acquisition acceleration factor.<sup>1–6</sup> Successful results with this recent technology,<sup>1,2,7,8</sup> especially in the human brain, have convinced several tens of top-level biomedical research centers throughout the world to acquire 7-T scanners; promising human brain MRI data have been obtained at 9.4-T,<sup>9–12</sup> and even higher field human

scanners are being built or installed for advanced neuroscience research.

Since its inception, MRI has operated in the long-wavelength (quasi-static) regime where radio-frequency (RF) wavelength is much larger than the imaged sample. With the advent of UHF-MR human imagers, however, given the high dielectric constant,  $\epsilon_r$ , of tissues, the excitation wavelength becomes on the order of, or smaller than, the imaged sample, resulting in a fairly complex mix of near-field and far-field RF behaviors. Namely, at  $B_0 = 7$  T, with  $\epsilon_r$  typically about 50–55 in biological samples at this Larmor frequency (~300 MHz), the RF wavelength inside tissues is about 14 cm or less. Owing to this short wavelength, complex RF phase modulation and interference phenomena, commonly observed at microwave and optical frequencies but traditionally negligible in MR experiments, are readily observed in tissues at UHF. In practice, biological tissues behave like lossy dielectrics, resulting in a complex superposition of multiple propagating mode excitations intermixed with RF penetration attenuation, yielding highly non-uniform excitation magnetic field ( $B_1$ ) distribution, an issue quickly identified as one of the main challenges to develop UHF-MR technology in humans.<sup>5,6,13–18</sup> Whereas in MR scanners operating at 3 T or lower magnetic field, the RF exciter is almost exclusively in the form of a whole body birdcage coil,<sup>19</sup> generating a homogeneous right-hand circularly polarized (CP) RF magnetic field, usually denoted as  $\mathbf{B}_1^+$ , using a volume RF coil at UHF, especially in the body, basically seems to be an impossible task. Notable attempts to generate a more uniform  $B_1^+$  field with a body coil at 7 T with a TEM body coil<sup>20</sup> were not successful. Twisting a birdcage volume coil structure toward a spiral shape<sup>21</sup> has been proposed to distribute RF phase through space; however, this was for head RF excitation and only at 4 T, thus in this instance, RF interactions were still dominated by a near-field or quasi-static regime.

Real breakthrough solutions for UHF-MR were demonstrated with the advent of RF coil arrays, based on loop, stripline or dipole elements, fed multi-channel RF technology such as  $B_1$  shimming and transmit SENSE,<sup>22–30</sup> triggering a large number of coil element designs to be compared, most of the latter still dominated by the near-field rather than far-field regime. Despite numerous multi-channel coil designs proposed, transmit  $\mathbf{B}_1$  ( $\mathbf{B}_1^+$ ) spatial heterogeneity and RF induced local tissue heating (specific absorption rate – SAR) are still dominant issues, responsible for the relatively limited scope of clinical applications pursued at 7 T and higher fields. In addition, it should be emphasized that coil arrays can be cumbersome to setup on a human body; namely, setting up a patient with multi-channel, high RF powered transmitter coil arrays surrounding the torso is far less simple than setting up arrays of receiver coils routinely utilized in standard clinical MR scans.

In an original approach that generated a lot of interest, a traveling-wave (TW) antenna was used and it was shown that RF signals could reach organs located quite far away from the antenna itself<sup>31</sup>; however, this technique was almost abandoned a few years later because of extremely low RF power efficiency.<sup>32</sup> It should be noted that most TW-based attempts in UHF MRI, trying to exploit far-field RF components and provide long ranged excitation profiles, used patch antennas that excite CP TW fields inside a scanner's bore.<sup>33</sup> This excitation, however, if not aided by additional electrodynamic elements (dielectrics or metamaterials), stay highly localized, resulting in rapid power dissipation in the body and quick attenuation with distance away from the antenna. It should also be noted that there are novel methods that can significantly improve the efficiency of conventional TW coils, at 7 T, such as using the dielectric pad placed “beyond” the region of interest<sup>34</sup> and the passive resonators in the form of local loop and dipole arrays.<sup>35</sup>

Overall, RF coil design for human UHF scanners remains an area of intense development,<sup>5,8,22,36</sup> especially regarding the most challenging targets, namely those requiring torso RF excitation,<sup>20,37–39</sup> also known as “body imaging.” Yet, some coil structures have not been thoroughly investigated. Helix antennas are well known for producing a CP field in their axial mode (in free space) while, at the same time, behaving as a TW antenna when considering the current traveling along the wire.<sup>40</sup> In fact, helix antennas have been proposed as TW CP sources for MR at 7 T with the imaged sample being positioned outside the helix.<sup>41,42</sup> Here, we introduce a radically different approach, aiming at exploiting the properties of the inner volume of a helix antenna to tackle the difficult issue of RF penetration at UHF.

We propose a novel category of multi-channel RF coil structures with volume coverage for UHF MRI, based on helix conducting elements, the helix coil, namely, subject-loaded multifilar helical-antenna RF volume coil, with its inner volume being utilized to image a sample. The new coil is initially designed according to the procedure set forth in,<sup>40</sup> for narrow band far-field operation, and then re-optimized to yield required near-field properties in the MRI bore. Namely, the new coil exploits the favorable near-field properties of the helix and allows for uniquely combining traveling-wave behavior through the overall coil wire structure while preserving near-field RF interaction between the inner side of the conducting elements and the imaged tissues.

The basic idea of the novel multi-channel helical-antenna inner-volume UHF-MR RF coil and initial results are preliminary presented in a summary form in.<sup>43–46</sup> A novel method for excitation of RF  $\mathbf{B}_1$  field in high-field MRI systems at  $B_0 = 3$  T using a subject-loaded quadrifilar (4-channel) helical antenna as an RF coil is proposed, evaluated, and demonstrated, by numerical simulations, in Ref. 47 The main differences of the 3-T coil in Ref. 47 with

respect to the UHF-MR helical-antenna RF coils, at  $B_0 = 7$  T ( $f_0 = 300$  MHz) and  $B_0 = 10.5$  T ( $f_0 = 443$  MHz), are as follows. The helical antenna in a 3-T MR bore, at an operating frequency of  $f_0 = 127.8$  MHz, is not a traveling-wave antenna, and the helix RF coil at 3 T is not a TW coil. It also does not operate in the axial mode of a helical antenna, but in the normal (“low-frequency”) mode. The 3-T helix coil does not support a far-field regime in the bore, or a combination of far- and near-field behaviors; it still is a near-field or quasi-static coil. In addition, the CP RF magnetic field,  $\mathbf{B}_1^+$ , of the quadrifilar helical-antenna RF coil in<sup>47</sup> is generated, essentially, by the four channels fed in time-phase quadrature, and not as the CP fields of the four individual helices, operating in the normal mode.

## 2 | MATERIALS AND METHODS

It is well known that helical antennas in their axial mode in free space (unbounded air-filled space), radiate a circularly polarized (CP), eg, right-hand CP (RCP), endfire beam, ie, RCP electromagnetic wave, along and near the helix axis far away from the helix.<sup>48,49</sup> In addition, the helical antenna is essentially a traveling-wave (TW) antenna — the current along the wire of the antenna, when operating in free space, behaves like a traveling current wave (except in the regions close to the beginning and the end of the helical winding). The expectation is that the TW current of the helical antenna, when placed in the MRI bore as an RF exciter and loaded with a phantom or a subject that is being imaged, will

produce — inside the phantom (subject) — an RF magnetic field  $B_1$  that is RCP and more spatially uniform than with other RF body coils, thereby further enabling large FOV ( $>30$  cm) clinical applications at UHF. Note that in other UHF attempts that also used helix coils at 7 T, the imaged sample was placed outside of the coil, and thereby exposed to the abovementioned extremely low RF power efficiency.<sup>41,42</sup>

Single-channel — or monofilar — (uniformly wound) helical antenna (in free space) is the simplest of all helical-antenna designs, summarized as a metallic wire antenna wound periodically with  $N$  wire turns and a pitch  $P$  about an imaginary (or dielectric) cylinder of diameter  $D_{\text{helix}}$  and length  $L_{\text{helix}} = NP$ ,<sup>40</sup> and shown as Helix 1 (a single filament) in Figure 1A. Instead of thin cylindrical wires, of radius  $r_w$ , one can use thin narrow strips, of width  $w_s$ , where the relationship between the two parameters for an approximately equivalent performance is given by  $r_w = w_s/4$ . The pitch  $P$  relates to the pitch angle,  $\alpha$ , as  $P = C_{\text{helix}} \tan \alpha$ , where  $C_{\text{helix}} = \pi D_{\text{helix}}$  is the helix circumference. The antenna is fed at one wire end against a circular back plate, Figure 1A, acting as a ground plane, ie, the input power is supplied at a lumped excitation port between the wire end and the plate. Taking advantage of the multi-channel RF technology available at 7 T and 10.5 T, we propose and present a more advanced RF coil design approach, based on either a quadrifilar (4-channel) or an octafilar (8-channel) helical antenna, where four (or eight) helices [eg, Helices 1-4 in Figure 1A] are wound coaxially and fed in time-phase quadrature, that is, with  $[360^\circ/M]$  phase increments ( $M = 4$  or 8, number of channels) with respect to each other in azimuthal order against the common

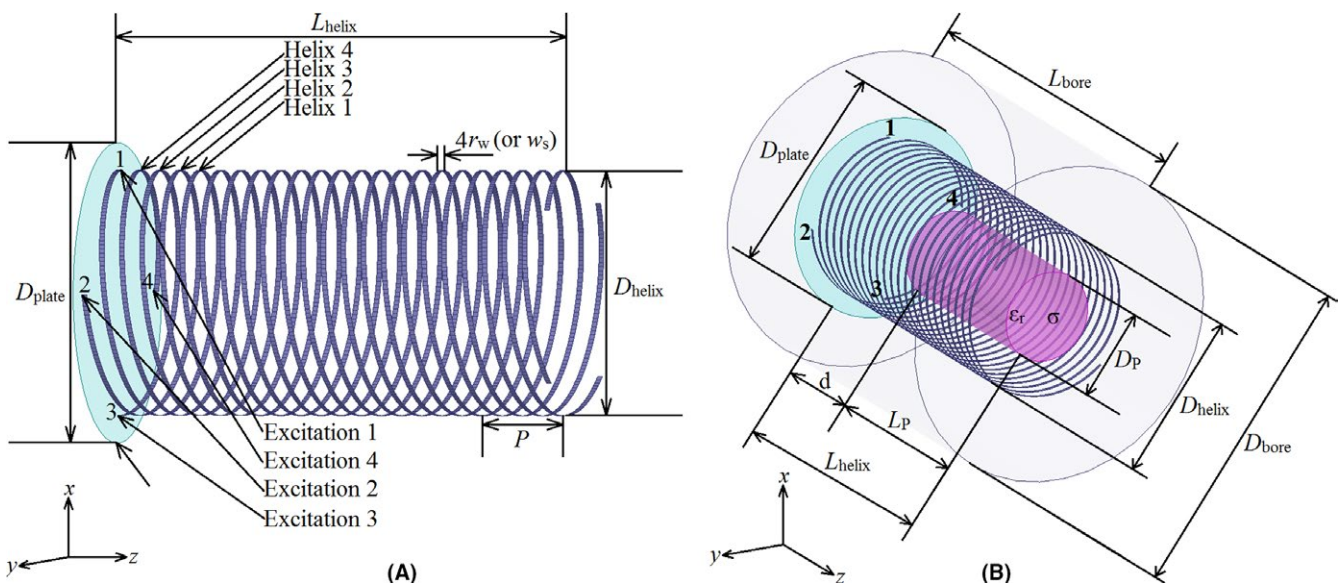


**FIGURE 1** (A) Sketch of a quadrifilar axial mode helical antenna in free space. The antenna consists of four helices (Helices 1-4) fed by four generators (Excitations 1-4)  $90^\circ$  out of phase with respect to each other against the common back plate (complex RMS voltages of the generators are  $V + j0$ ,  $0 - jV$ ,  $-V + j0$ , and  $0 + jV$ , respectively, where  $j = \sqrt{-1}$  is the imaginary unit). (B) Higher order MoM-SIE simulation model of an UHF MRI metallic bore with a 4-channel RF volume coil in the form of a phantom-loaded helical antenna

back plate. Note that in,<sup>47</sup> the 3-T quadrifilar helical-antenna coil cannot produce a CP RF magnetic field without being fed in quadrature. Namely, at 3 T ( $f_0 = 127.8$  MHz), a monofilar helical-antenna RF coil does not produce a CP magnetic field at its axis. On the other hand, at UHF (eg, 7 T and 10.5 T), each helical arm produces a CP RF magnetic field along its axis even if operated individually. Driving the four arms of a 7-T or 10.5-T quadrifilar helix in quadrature enhances this effect. The goal of this multi-channel approach is to enable multi-channel RF methods (eg,  $B_1$  shimming) to further mitigate  $B_1^+$  field heterogeneity.

Design of the proposed multifilar helical-antenna exciters, as well as analysis of the RF electromagnetic field in 7-T and 10.5-T MRI bores generated by the exciters, is based on mathematical modeling and simulation using computational electromagnetics (CEM) techniques that rigorously take into account the geometry and material composition of the structure and include all field and wave effects by numerically solving the underlying Maxwell's equations and associated field boundary conditions at any frequency.<sup>50</sup> Specifically, modeling and analysis of the MRI structures are performed using a full-wave numerically rigorous CEM technique based on the method of moments (MoM) in conjunction with the surface integral equation (SIE) approach,<sup>51</sup> implemented in a numerically higher order fashion.<sup>52</sup> In this technique, all material (metallic and dielectric) surfaces in the structure are modeled using generalized parametric quadrilateral patches and all metallic wires are modeled by means of straight wire segments, electric and magnetic equivalent surface currents over elements (quadrilateral patches and wire segments) are modeled by polynomial vector basis functions, and SIEs based on boundary conditions for electric and magnetic field vectors are solved employing Galerkin method.<sup>51</sup> In addition, the results obtained by the higher order MoM-SIE technique are thoroughly verified and validated by comparison with results using two well-established commercial full-wave CEM codes, a MoM code WIPL-D<sup>53</sup> and a finite element method (FEM) code ANSYS-HFSS.<sup>54</sup>

To demonstrate the novel method for RF excitation at UHF using a subject-loaded helical antenna as an RF exciter,

shown in Figure 1B is an UHF-MR system with a bore in the form of a metallic cylinder of diameter  $D_{\text{bore}}$  and length  $L_{\text{bore}}$  (simplified model of a clinical scanner). Computations and experiments are performed on a phantom in the form of a cylinder of diameter  $D_p$  and length  $L_p$  filled with a homogeneous lossy dielectric of relative permittivity (dielectric constant)  $\epsilon_r$ , conductivity  $\sigma$ , and relative permeability (magnetic constant)  $\mu_r = 1$ . The RF magnetic field  $B_1$  in the bore and in the phantom is excited by a phantom-loaded quadrifilar helical antenna, of diameter  $D_{\text{helix}}$  and length  $L_{\text{helix}}$ , with the pitch and wire radius (strip width) of each of the four helices being  $P$  and  $r_w$  ( $w_s$ ), respectively, placed coaxially with respect to the bore and fed as in Figure 1B, against the back plate of diameter  $D_{\text{plate}}$ , at an operating frequency  $f_0$ . The phantom is placed coaxially with the helical-antenna coil and the bore at a distance  $d$  from the back plate.

We have designed and fabricated several quadrifilar (4-channel) and octafilar (8-channel) helical-antenna RF coil prototypes at 7 T and 10.5 T, respectively, in Electromagnetics Laboratory at Colorado State University, as depicted in Figures 2 and 3. The prototypes are a 4-channel helical-antenna coil at 7 T ( $L_{\text{helix}} = 60$  cm,  $D_{\text{helix}} = 32$  cm), shown in Figure 3A, an 8-channel 7-T coil ( $L_{\text{helix}} = 65$  cm,  $D_{\text{helix}} = 32$  cm), Figure 3B, a 4-channel coil at 10.5 T ( $L_{\text{helix}} = 60$  cm,  $D_{\text{helix}} = 21$  cm), Figure 3C, and an 8-channel 10.5-T coil ( $L_{\text{helix}} = 60$  cm,  $D_{\text{helix}} = 21$  cm). In these prototypes, the individual helical spirals are narrow strips ( $w_s = 6$  mm) realized from a 35- $\mu\text{m}$  thick copper tape, and the weights are  $\sim 11.3$  kg and  $\sim 6.8$  kg for the 7-T and 10.5-T prototypes, respectively.

Another interesting feature of our designs is that in all helical-antenna RF coil prototypes we designed and built, the exciters are internally matched and they do not need any matching circuits — in free space, outside of the MRI bore and prior to being loaded with a phantom or subject. This is done, at both 7 T and 10.5 T, by including specially designed matching plates at each of the four/eight helices [each plate is about a quarter/eighth of the helix circumference long and starts right after the respective connector (excitation port) and ends right before the next port in a quadri/octafilar

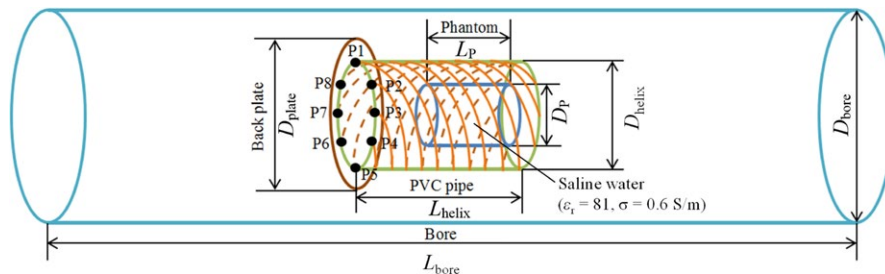


**FIGURE 2** Sketch of an octafilar (8-channel) phantom-loaded helical-antenna UHF (at 7 T and 10.5 T, respectively) MRI RF volume coil prototype, with  $M$  helices wound coaxially and fed  $360^\circ/M$  phase increments ( $M = 8$ ) against the common back plate (ports P1-P8), used in CMRR experiments; saline-water cylindrical “bottle” phantom is at the far end inside the coil

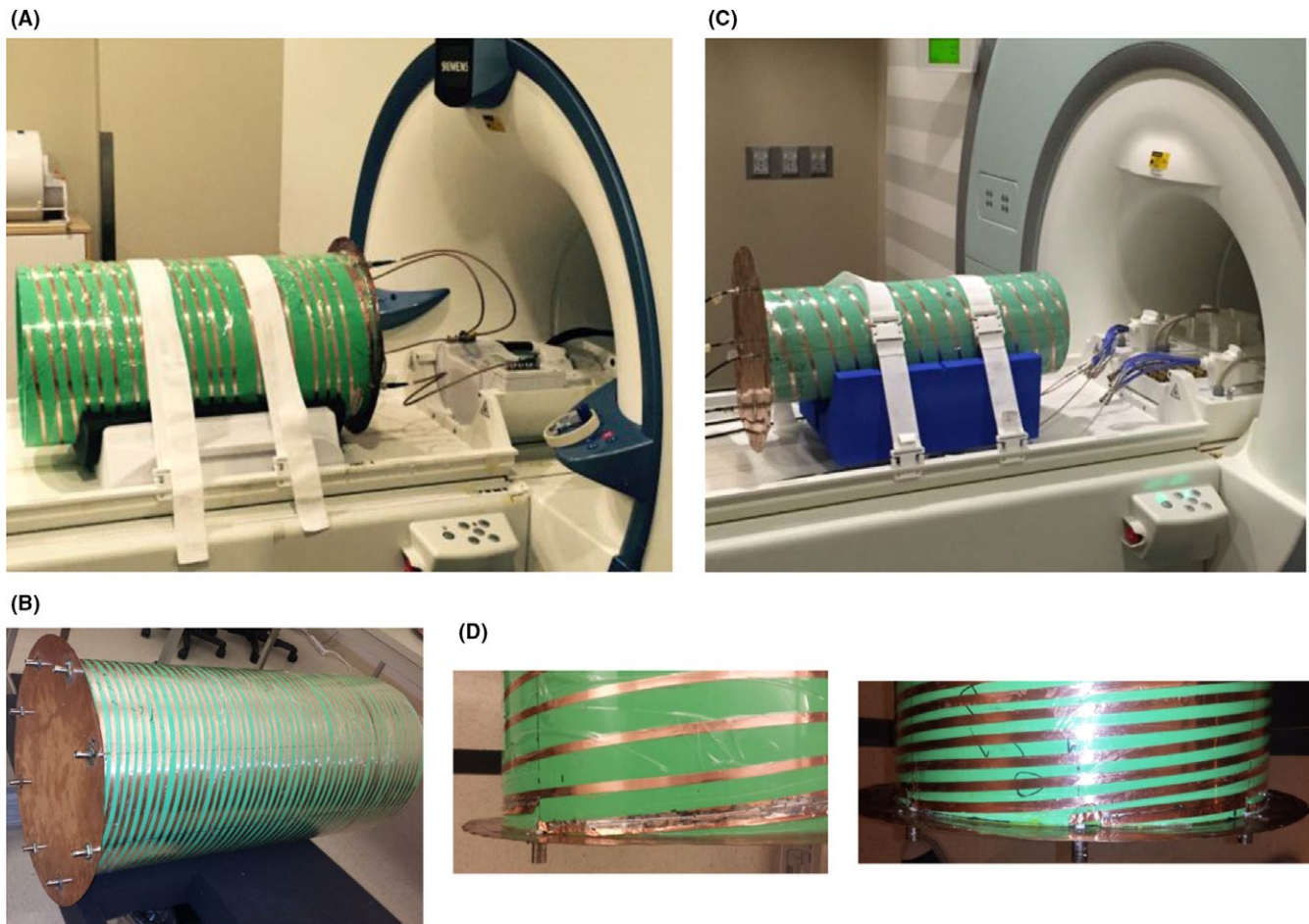


**FIGURE 3** (A) Multi-channel helical-antenna inner-volume RF coil prototypes during CMRR experiments: (A) 4-channel ( $M = 4$ ) 7-T, 300-MHz, prototype (Figure 1), (B) 8-channel ( $M = 8$ ) 7-T, 300-MHz, prototype (Figure 2), (C) 4-channel 10.5-T, 443-MHz, prototype (Figure 1), and (d) specially designed matching plates at each of the four/eight helices of the 4-channel (left) and 8-channel (right) 7-T prototypes — internally matched antennas in free space

antenna arrangement], as shown in Figure 3D. Variation of widths and lengths of the matching plates together with fine tuning of coil wire (strip) lengths, is conducted to optimally match the coils internally, before further tuning the coil once placed in the scanner bore and loaded for MRI experiments. The return loss, measured in free space, is better than 10 dB for all ports, for all quadrifilar coils, and better than 8 dB for all ports, for all octafilar coils. Hence, the reflected power is only 10% or 15% or less in all cases. In addition, the coupling between the channels is below  $-10$  dB for both quadrifilar and octafilar helical-antenna coils. In general, by tuning the matching at the ports, input VSWR (voltage standing wave ratio) can always be kept below 2 for quadrifilar helices and below 2.5 for octafilar helices.

The helical-antenna RF coil prototypes are tested, validated, and evaluated experimentally in 7-T and 10.5-T MR scanners at the Center for Magnetic Resonance Research (CMRR), University of Minnesota [see Figures 3A,C, and 5A]. The MRI experiments are performed using phantoms in the form of a cylindrical “bottle” filled with saline water

[see Figure 5A], and using the phantom-loaded multi-channel helix coil as a transceiver (Tx and Rx simultaneously). Saline-water phantoms are standard phantoms used at the CMRR. Moreover, some of the examples from the literature, used here for comparison, also employ saline-water phantoms. The saline solution, although not an ideal substitute for human tissue, is an excellent medium widely used to observe the mode structures in UHF MRI. The electrical properties of the saline solution are such that they efficiently model the loss and small enough wavelengths arising from its high permittivity. In the saline solution, whose permittivity is higher than or equal to any other material tissue inside a human body, the wavelength is smaller than the wavelength in the human body, so it provides a worst case scenario.

The RF coil used in the analysis with the human body model presented in the article is 54 cm wide. The narrower helix RF coils characterized in the article are presented either in comparison with coils from the literature adopting the same/similar coil sizes or as an illustration of potential head imaging or other non-body imaging or as a step in the

direction of exploring wider RF coils using the multifilar helical-antenna design.

### 3 | RESULTS AND DISCUSSION

As the first structure within the presented framework of multi-channel helical-antenna inner-volume RF coils, we consider a 7-T MRI system as shown in Figure 1. Figure 4 shows experimentally and numerically obtained data for a 4-channel helical-antenna 7-T RF coil prototype with a “bottle” phantom (Figure 1:  $L_{\text{bore}} = 336$  cm,  $D_{\text{bore}} = 90$  cm,

$L_{\text{helix}} = 60$  cm,  $D_{\text{helix}} = 32$  cm,  $P = 10.7$  cm,  $w_s = 6.35$  mm,  $D_{\text{plate}} = 38$  cm,  $f_0 = 300$  MHz,  $L_p = 37$  cm,  $D_p = 17$  cm,  $\epsilon_r = 81$ ,  $\sigma = 0.6$  S/m), depicted in Figure 3A. The phantom is placed at the far end inside the RF coil ( $d = 22$  cm), as in Figure 2. The return loss, measured in free space, amounts to 13 dB, 10.61 dB, 28.72 dB, and 14.41 dB, respectively, at the four ports of the antenna prototype at  $f_0 = 300$  MHz w.r.t.  $50 \Omega$ . Shown in Figure 4 are CMRR-measured and simulated central coronal and axial  $B_1$  maps of the phantom, along with measured relative  $B_1$  field distributions in four different coronal slices with all four channels transmitting together. More specifically, Figures 4B and C show the

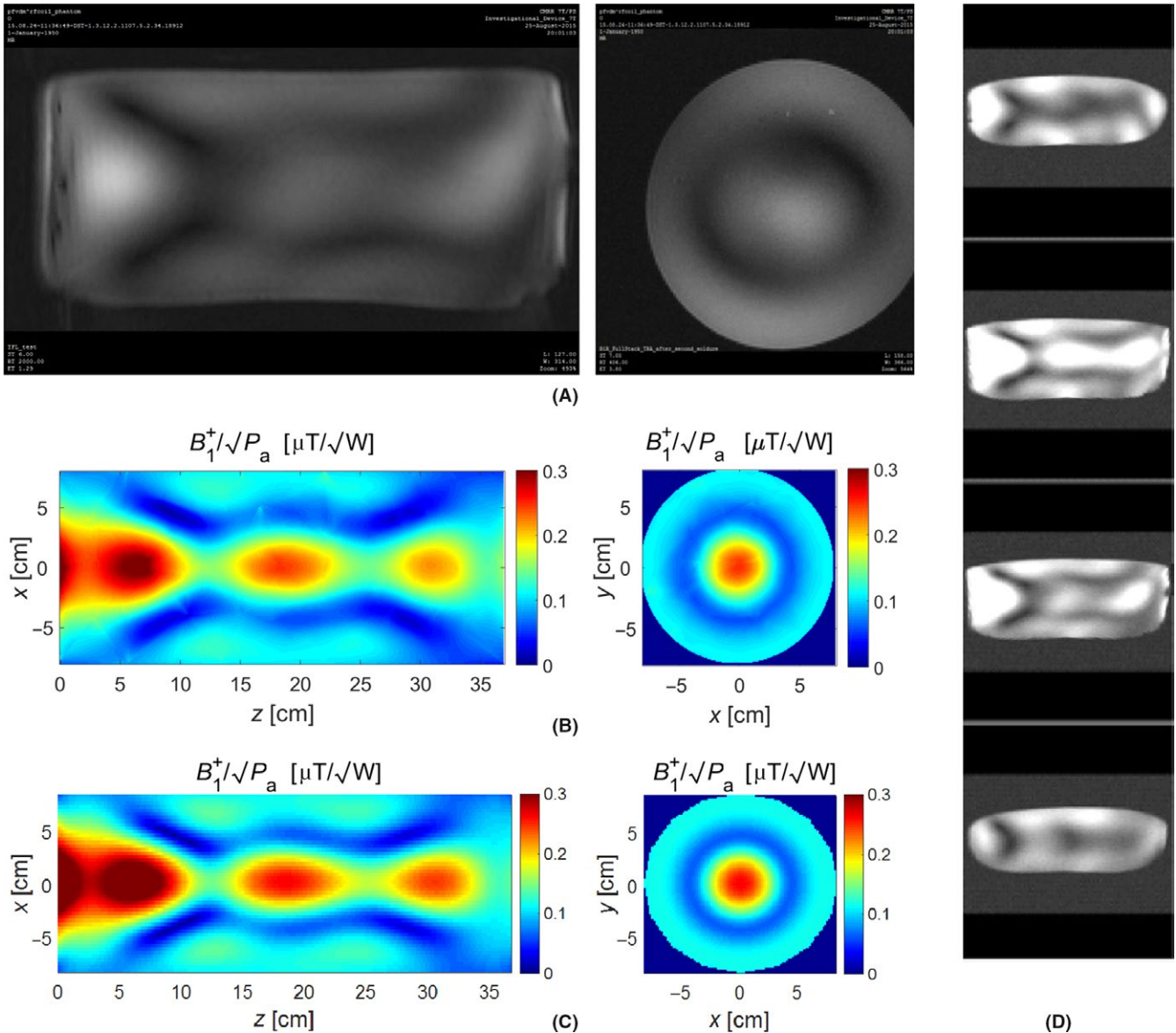


**FIGURE 4** Experimental and simulated central coronal and axial 2-D  $B_1$ -maps for a 4-channel helical-antenna 7-T RF coil prototype, in Figure 3A, with a saline-water “bottle” phantom placed at the far end inside the coil (as in Figure 2): (A) CMRR measurements (relative maps), (B) ANSYS-HFSS-computed  $B_1^+ / \sqrt{P_a}$  (transmit efficiency), and (C) MoM-SIE-computed  $B_1^+ / \sqrt{P_a}$  (transmit efficiency) in coronal and axial planes, respectively ( $P_a$  is the total accepted power); the computed maximum efficiency should be compared with the efficiencies in.<sup>32,55–57</sup> (D) CMRR-measured relative  $B_1$  field distributions in four different coronal slices with all four channels transmitting together

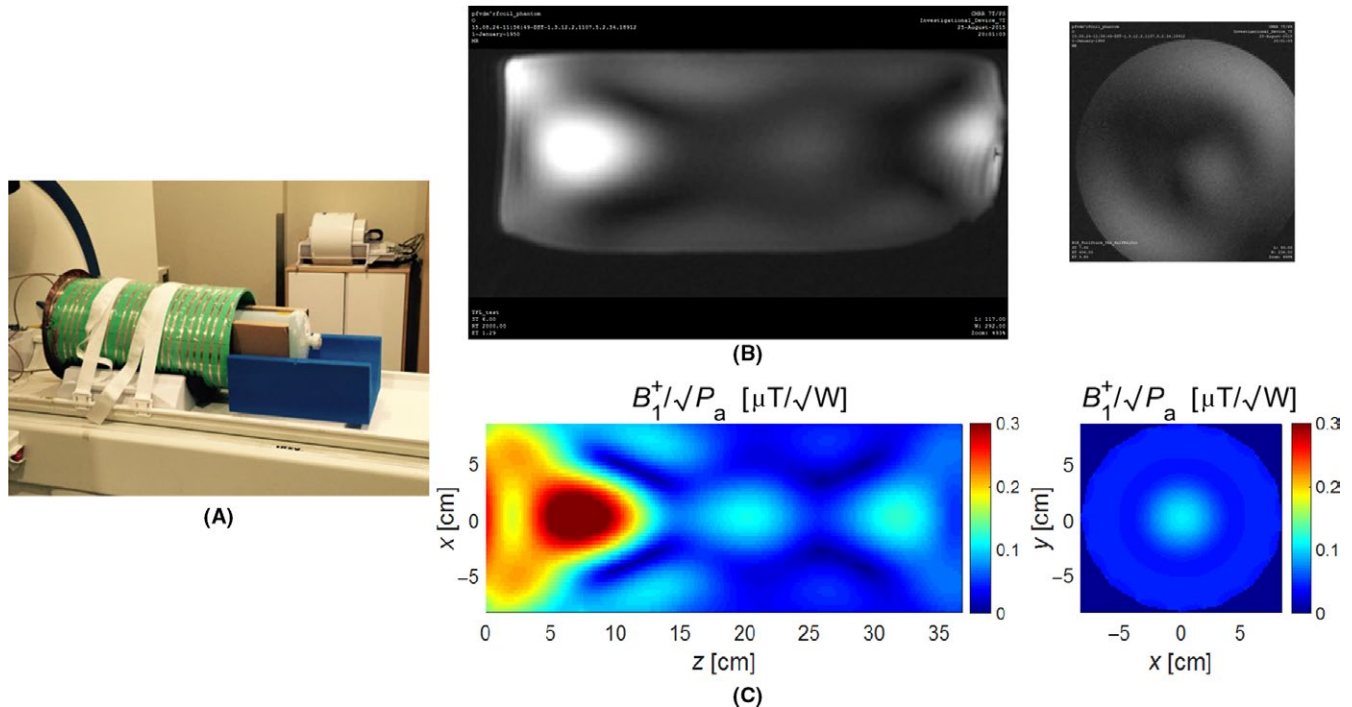


**FIGURE 5** (A) CMRR experiments at 7 T with the saline-water “bottle” phantom placed half inside and half outside the 4-channel helical-antenna RF coil prototype. (B) CMRR  $B_1$  measurements (relative maps). (C) MoM-SIE-computed  $B_1^+/\sqrt{P_a}$  (transmit efficiency) in coronal and axial planes of the phantom

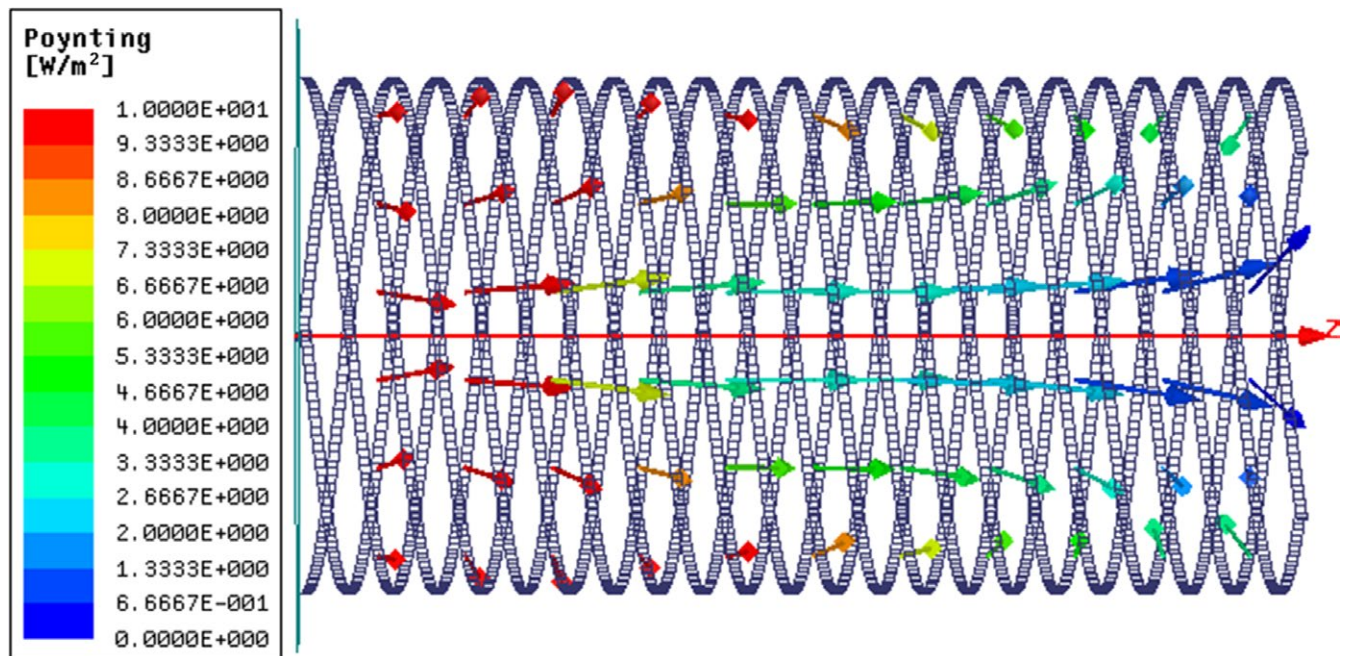


**FIGURE 6** Simulated Poynting vector in the coronal plane inside an unloaded 4-channel helical-antenna RF coil at 7 T

transmit efficiency evaluated using ANSYS-HFSS (FEM, volumetric, field modeling, code) and MoM-SIE (MoM, surface, current modeling, code), respectively, as  $B_1^+/\sqrt{P_a}$ , in coronal and axial planes, where  $P_a = P_{a1} + P_{a2} + P_{a3} + P_{a4}$  is the total accepted power for the coil, with  $P_{ai}$  standing for

the individual power accepted by the  $i$ -th coil ( $i = 1, 2, 3, 4$ ). We observe qualitative agreements between the two sets of simulation results obtained using two completely different computational techniques and between simulation results and measurements. The measured power efficiency is acceptable

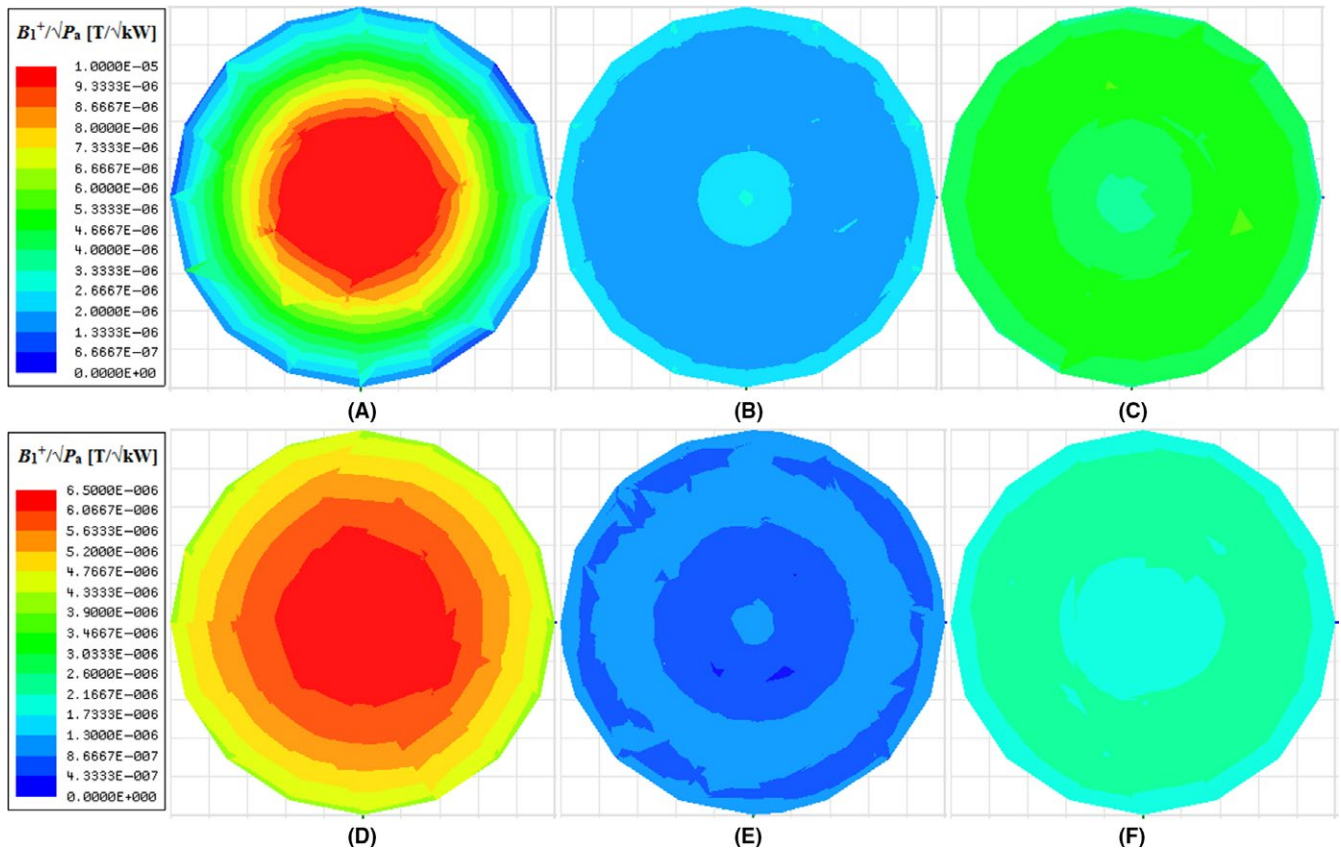


**FIGURE 7** Simulated axial 2-D  $B_1^+/\sqrt{P_a}$  efficiency maps for the 4-channel helical-antenna coil at 7 T loaded with a cylindrical saline-filled phantom, with (A-C) the entire phantom inside the RF coil and (D-F) half of the phantom inside and half outside the coil, for cuts at (A,D) the proximal end, (B,E) the central location, and (C,F) the distant end, respectively. The maximum  $B_1^+/\sqrt{P_a}$  efficiency results should be compared with those in Figure 4 of <sup>32</sup> for a standard traveling-wave setup

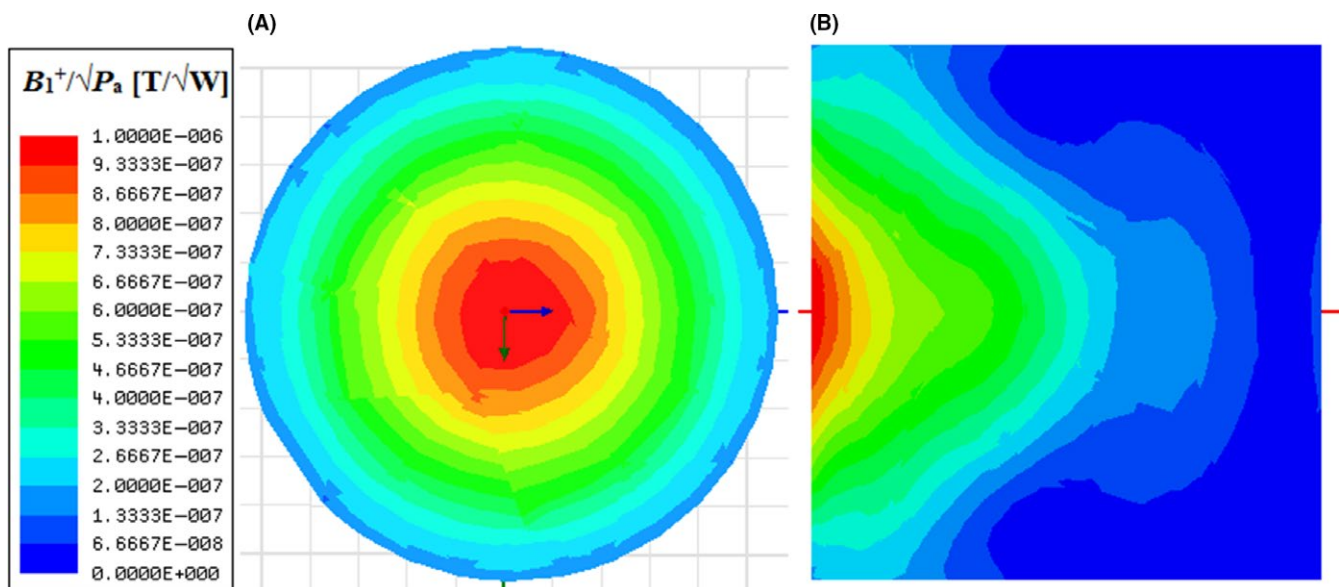


**FIGURE 8** Simulated (A) proximal-end axial and (B) sagittal 2-D  $B_1^+/\sqrt{P_a}$  efficiency maps of a cylindrical phantom as in <sup>58</sup> placed inside a 4-channel 7-T helical-antenna coil. The maximum  $B_1^+/\sqrt{P_a}$  efficiency should be compared with that in figure 12 of Ref. 58 for the microstrip transmission line (MTL) coil



and the amount of power delivered to the imaged phantom is sufficiently high for all experiments and MRI processing. The computed maximum efficiency is comparable with those reported for other state-of-the-art coils at 7 T in.<sup>32,55–57</sup>

Figure 5 shows the experimental and simulation results, namely, CMRR-measured relative  $B_1$  distribution and MoM-SIE-simulated  $B_1^+/\sqrt{P_a}$  efficiency maps, for the phantom placed half inside and half outside the coil ( $d = 41$  cm). For this phantom placement, the power delivered to the half of the phantom inside the helix is noticeably higher than the power delivered to the half that is outside. On the other hand, these results demonstrate the far-field component of the  $B_1$

field as it excites spins outside the coil volume. In addition, when the phantom is placed completely outside the coil, at its opening ( $d = 60$  cm), the power delivered to the phantom is still sufficient but considerably lower than when the phantom is completely inside the coil.

Figure 6 shows simulation results for the Poynting vector inside the 4-channel ( $M = 4$ ) 7-T helical-antenna RF coil described in the previous case but without any phantom inside the coil. The Poynting vector, for the most of the region inside the coil, is strongly aligned along the  $z$ -direction, indicating an overall forward traveling wave inside the antenna volume. This demonstrates utilization of the principles of a

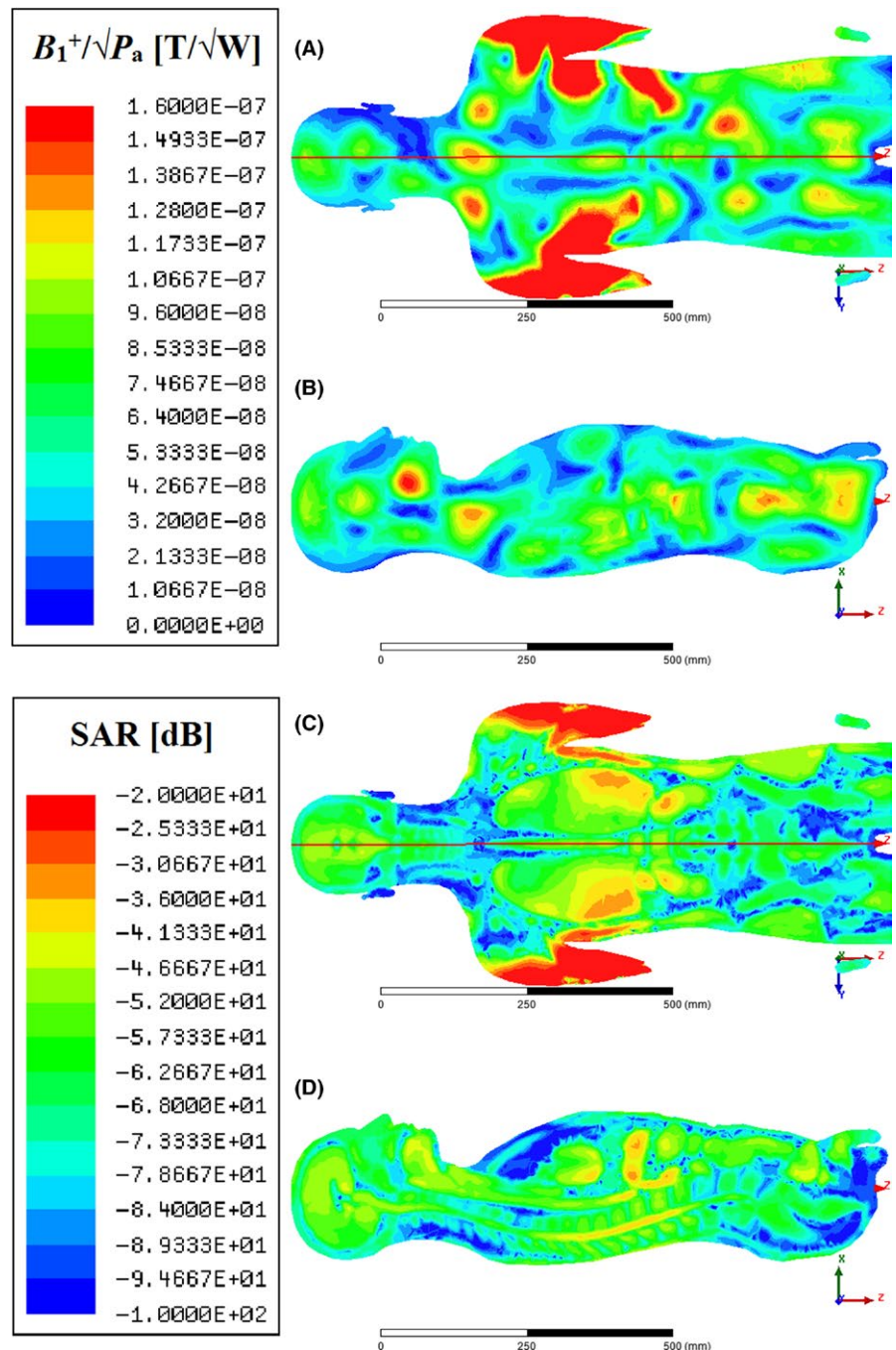


**FIGURE 9** Illustration of the potential applicability of the helical-antenna coil as a volume body UHF coil: simulation results for (A) coronal  $B_1^+/\sqrt{P_a}$  efficiency map, (B) sagittal  $B_1^+/\sqrt{P_a}$  efficiency map, (C) coronal SAR map, and (D) sagittal SAR map of an inhomogeneous realistic human body model placed inside a wider variant of the 4-channel 7-T helix coil. The  $B_1^+/\sqrt{P_a}$  efficiency and SAR results should be compared with those reported in Figures 9 and 11, respectively, in<sup>55</sup> for a similar human body model

traveling-wave MRI coil, that is, it shows that the coil is a traveling-wave antenna.

We then compare the efficiency of the helical-antenna design with some of the conventional and state-of-the-art designs at 7 T. We first compare our design with that of Brunner et al.,<sup>32</sup> which may be considered a standard traveling-wave setup. Figure 7 shows simulation results for  $B_1^+/\sqrt{P_a}$  efficiency maps of a 4-channel helical-antenna coil in axial cuts at three positions, namely, at the proximal end, central location, and distant end. The coil is the same as in the previous case and it is loaded by a cylindrical saline-filled phantom with  $L_p = 34$  cm,  $D_p = 10$  cm,  $\epsilon_r = 81$ , and  $\sigma = 0.84$  S/m in Figure 1B. Figures 7A-C show  $B_1^+/\sqrt{P_a}$  efficiency maps for the phantom placed at a distance  $d = 16.1$  cm from the back plate, with the entire phantom inside the RF coil, while Figures 7D-F show efficiency maps for the phantom placed at a distance  $d = 43.1$  cm from the back plate, with half of the phantom inside and half outside the coil. The maximum  $B_1^+/\sqrt{P_a}$  efficiencies in both these cases are similar and comparable to the efficiency shown in figure 4 of Ref. 32

Next, shown in Figure 8 are simulation results for proximal-end axial and sagittal  $B_1^+/\sqrt{P_a}$  efficiency maps of a 4-channel 7-T helical-antenna design (Figure 1:  $L_{\text{bore}} = 336$  cm,  $D_{\text{bore}} = 90$  cm,  $L_{\text{helix}} = 30$  cm,  $D_{\text{helix}} = 27$  cm,  $P = 10.67$  cm,  $w_s = 6.35$  mm,  $D_{\text{plate}} = 40$  cm,  $f_0 = 300$  MHz) aimed for comparison with the results of the microstrip transmission line (MTL) coil shown in Sohn et al.<sup>58</sup> (their figure 12). The phantom inside the helix coil is modeled to mimic the cylindrical phantom from<sup>58</sup> as accurately as possible with  $L_p = 21$  cm,  $D_p = 22$  cm,  $\epsilon_r = 58.1$ , and  $\sigma = 0.539$  S/m in Figure 1B, and is positioned at a distance  $d = 9.1$  cm from the back plate, that is, at the far end of the helix (the far end of the phantom is at the far end of the coil). Note that this case also represents a potential head imaging situation. We see that the maximum  $B_1^+/\sqrt{P_a}$  efficiency of the helical-antenna coil in Figure 8, being  $1.15 \mu\text{T}/\sqrt{\text{W}}$ , is comparable to that of the MTL coil.<sup>58</sup>

In order to demonstrate the applicability of the helical-antenna coil as a volume body UHF coil, Figures 9A and B show simulation results for  $B_1^+/\sqrt{P_a}$  efficiency maps of a wider variant of the 4-channel 7-T helical-antenna coil design,

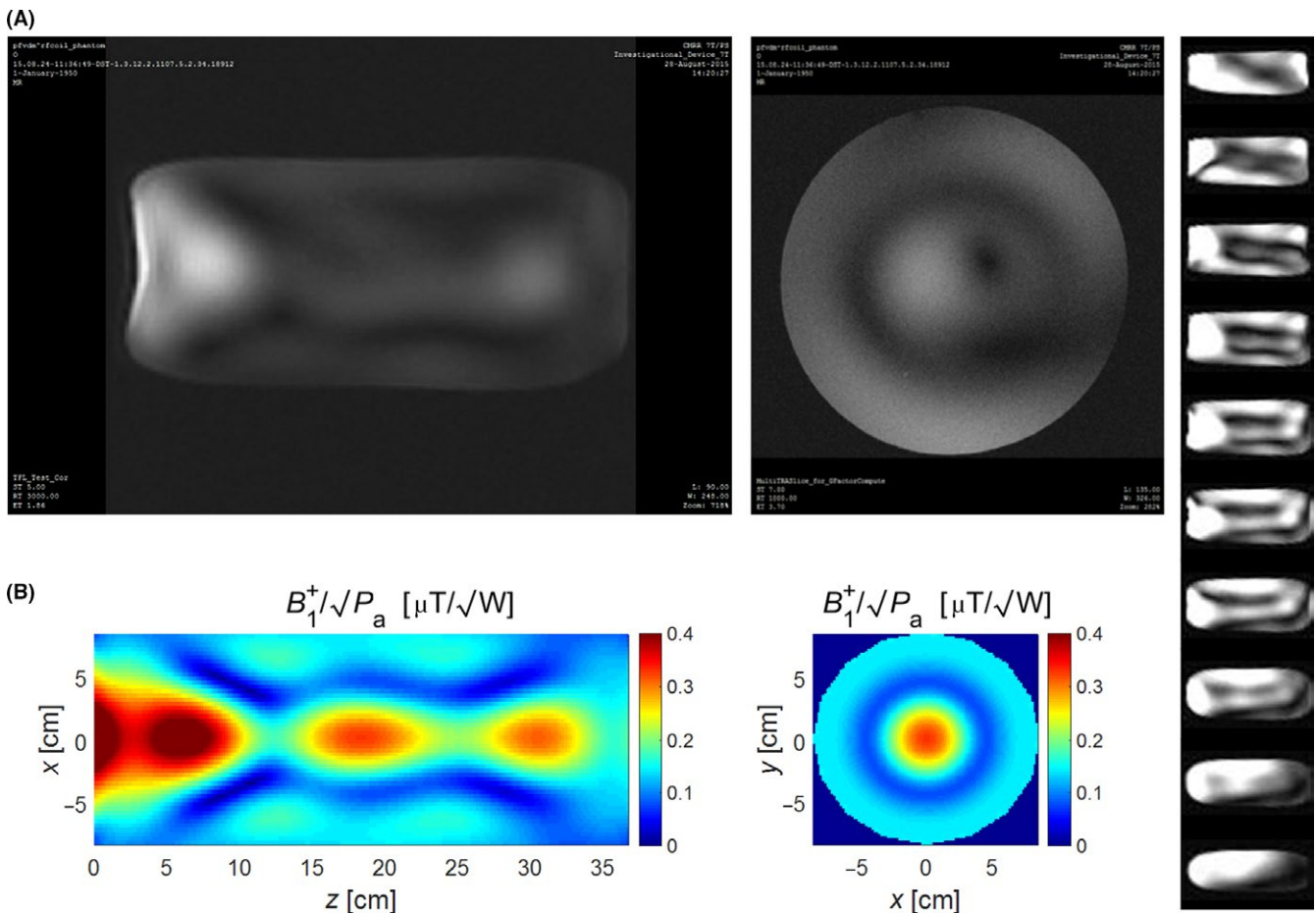


**FIGURE 10** (A) CMRR-measured relative  $B_1$  maps and (B) MoM-SIE-simulated  $B_1^+/\sqrt{P_a}$  efficiency maps in central coronal and axial planes for an octafilar (8-channel) helical-antenna coil prototype at 7 T, in Figure 3B, with the saline-water “bottle” phantom placed at the far end inside the coil (Figure 2). (C) Experimental relative  $B_1$  field distributions in ten different coronal slices with all eight channels transmitting together

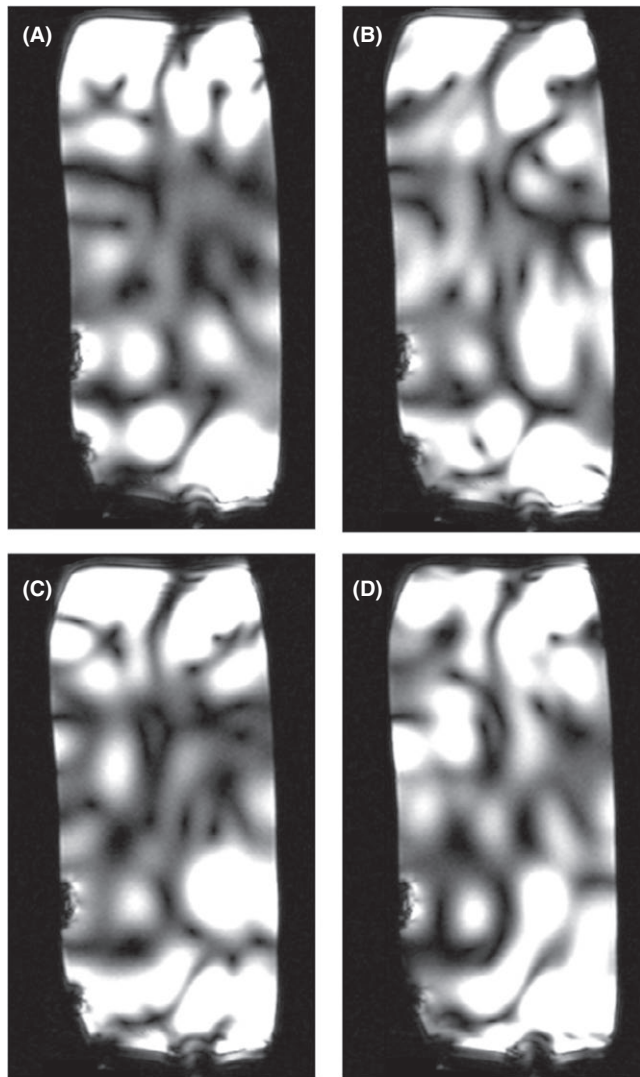


**FIGURE 11** CMRR-measured relative  $B_1$ -maps for a 4-channel helical-antenna RF coil prototype at 10.5 T, in Figure 3C, with the saline-water “bottle” phantom placed at the far end inside the coil (as in Figure 2): (A–D) magnitude image (GRE, sagittal slice) from each of the four receive channels (RF transmission on all channels without specific transmit phase adjustment)

namely, of a 54-cm wide helix (Figure 1:  $L_{\text{bore}} = 336$  cm,  $D_{\text{bore}} = 90$  cm,  $L_{\text{helix}} = 60$  cm,  $D_{\text{helix}} = 54$  cm,  $P = 10.67$  cm,  $w_s = 6.35$  mm,  $D_{\text{plate}} = 60$  cm,  $f_0 = 300$  MHz), loaded with a human body model. The model used for the simulation is a detailed inhomogeneous layered model of a human body made of 30 different lossy dielectrics (plus air) for various tissues, cavities, fluids, etc. The model is that of a male human and is 183 cm (6 feet) at its longest, that is, from the head top to feet bottom, and 52 cm at its widest, that is, from one arm to the other. The body model is placed inside the coil at a distance  $d = 6$  cm away from the back plate. The  $B_1^+/\sqrt{P_a}$  efficiency results are similar and comparable in value and distribution to those calculated from the results and input power of Zhang et al<sup>55</sup> in their Figure 7, where a similar human body

model was used and it was shown that the  $B_1^+$  field is sufficient for successful imaging. Moreover, it can be seen from Figures 9A and B that the field efficiency in the bulk of the torso is higher in the case of the helical antenna, that is,  $\sim 0.09$   $\mu\text{T}/\sqrt{\text{W}}$ , compared to  $\sim 0.075$   $\mu\text{T}/\sqrt{\text{W}}$  in<sup>55</sup> (Figure 9). With reference to the SAR maps shown in Figures 9C and D, we can see that the SAR values for the helical-antenna coil are for the most part lower than or equal to those of Zhang et al<sup>55</sup> in their Figure 11.

Figure 10 shows CMRR-measured relative  $B_1$  distribution and MoM-SIE-simulated  $B_1^+/\sqrt{P_a}$  efficiency maps in the central coronal and axial slices for an octafilar, 8-channel ( $M = 8$ ), helical-antenna coil prototype at 7 T (Figures 1 and 2:  $L_{\text{bore}} = 336$  cm,  $D_{\text{bore}} = 90$  cm,  $L_{\text{helix}} = 65$  cm,  $D_{\text{helix}} = 32$  cm,  $P = 10.7$  cm,  $w_s = 6.35$  mm,  $D_{\text{plate}} = 38$  cm,  $f_0 = 300$  MHz,  $L_p = 37$  cm,  $D_p = 17$  cm,  $\epsilon_r = 81$ ,  $\sigma = 0.6$  S/m,  $d = 22$  cm), depicted in Figure 3B, as well as the measured  $B_1$  field distributions in ten different coronal slices with all eight channels transmitting together. Similar observations, as for Figure 4, are made, from Figure 10, for the 8-channel helical-antenna 7-T coil. The computed transmit efficiency of the octafilar helix is better than that of the quadrifilar one.

As the last structure, we consider a 4-channel helical-antenna RF coil prototype at 10.5 T with the saline-water “bottle” phantom placed at the far end inside the coil (Figures 1 and 2:  $M = 4$ ,  $L_{\text{bore}} = 410$  cm,  $D_{\text{bore}} = 90$  cm,  $L_{\text{helix}} = 60$  cm,  $D_{\text{helix}} = 21$  cm,  $P = 16$  cm,  $w_s = 6.35$  mm,  $D_{\text{plate}} = 38$  cm,  $f_0 = 443$  MHz,  $L_p = 37$  cm,  $D_p = 17$  cm,  $\epsilon_r = 81$ ,  $\sigma = 0.6$  S/m,  $d = 22$  cm), shown in Figure 3C. The free-space return loss w.r.t.  $50 \Omega$  is measured, at  $f_0 = 443$  MHz, to be 10.63 dB, 11.83 dB, 14.48 dB, and 20.4 dB, respectively, at the four ports of the antenna prototype. Shown in Figure 11 are the results from CMRR experiments for the relative  $B_1$  field distribution in the sagittal cross section of the phantom — magnitude images from each of the four receive channels, with RF transmission on all channels. Note that 10.5-T experiments are done without proper phasing of the four excitation ports of the coil, with which circular polarization would be further enhanced. Overall, experimental results at 10.5 T demonstrate the scalability and versatility of the UHF-MR helix coil design.

## 4 | CONCLUSIONS

This article has proposed a novel category of multi-channel RF coil structures with volume coverage for UHF MRI based on a subject-loaded multifilar helical-antenna exciter. The main outcome of the multi-channel helical-antenna inner-volume coil development is to provide improved RF performance for UHF MRI while preserving the easiness of use of a volume coverage coil. The inner volume of a helical-antenna structure is utilized to image a sample (conventional helix

coils are utilized as a TW CP source with the target sample outside of the coil). This design benefits from the congruence of two regimes: a far-field regime that concerns the current path over the wires of the coil and a near-field regime that is involved in local interactions between the sample and the coil wires. Furthermore, multiple channels are utilized (4 and 8 in the prototype configurations) to enable all multi-transmit channel RF technology.


The presented phantom data obtained at 7 T show good qualitative consistency between numerical simulations and experimental results with 4- and 8-channel helix coils. The numerical results for the maximum  $B_1^+/\sqrt{P_a}$  efficiency of helical-antenna RF coils are comparable to or higher than those of some of the conventional and state-of-the-art coil designs at 7 T. The 10.5-T machine at CMRR used for this work is the first (and only, as of today) operational human-size MRI scanner reaching 10.5 T. The experimental results show the scalability of the helix coil design to 10.5 T.

Our future work will also include further characterization and quantification of RF efficiency, SAR distribution, and spatial  $B_1^+$  encoding of the novel 4- and 8-channel helix RF UHF-MR volume coils in phantom experiments and in simulations. It will also include further improvements of the designs; namely, the proposed and presented framework of multi-channel helix coils provides ample room for further RF coil design optimization. Using systematic variation of antenna parameters, with the focus on the near-field operation inside the antenna structure, parameters that can be considered in optimization include the helix circumference, pitch, length (number of turns), wire thickness (strip width), additional lumped impedance loads along the way, number of channels, position of the coil in the bore, and position of the phantom with respect to the coil and the bore, as well as many other parameters and modifications of the structure. Furthermore, flexible and wearable helical-antenna RF coils are also possible. In addition to using the helix coil as a transceiver, as in experiments in Figures 4, 5, 10, and 11, our future work will also include demonstration of the new coil as transmit only body coil, with various surface coils as receive coils, which will require proper detuning of the helix using PIN diodes. This could increase the SNR and hence the quality of the image. Another possible improvement is to change the helical-antenna inner-volume coil designs so to include a mesh or slotted back plate or a hollow back plate (metallic ring) — to eliminate or significantly reduce any surface eddy currents induced on the copper back plate in Figures 1–3. Namely, the large continuous solid back plate is prone to creating strong eddy currents during fast gradient coil switches occurring during MR scans, which can translate into signal losses and spatial distortion when a sample is too close to the plate, and can potentially generate acoustic noise due to vibrations.

## ACKNOWLEDGMENT

This work was supported by the National Science Foundation under grant ECCS-1307863 and by the Serbian Ministry of Education, Science, and Technological Development under grant TR-32005.

## ORCID

Milan M. Ilić  <https://orcid.org/0000-0003-4196-3594>

Branislav M. Notaroš  <https://orcid.org/0000-0002-5755-961X>

## REFERENCES

1. Ugurbil K, Adriany G, Andersen P, et al. “Ultrahigh field magnetic resonance imaging and spectroscopy”. *Magn Reson Imaging* 2003;21(10):1263-81.
2. Ugurbil K. Magnetic resonance imaging at ultrahigh fields. *IEEE Trans Biomed Eng.* 2014;61(5):1364-79.
3. Wiesinger F, Van de Moortele PF, Adriany G, De Zanche N, Ugurbil K, Pruessmann KP. “Parallel imaging performance as a function of field strength—an experimental investigation using electrodynamic scaling”. *Magn Reson Med* 2004;52(5):953-64.
4. Wiesinger F, Van de Moortele PF, Adriany G, De Zanche N, Ugurbil K, Pruessmann KP. “Potential and feasibility of parallel MRI at high field”. *NMR Biomed* 2006;19(3):368-78.
5. Vaughan JT, Garwood M, Collins CM, et al. “7T vs. 4T: RF power, homogeneity, and signal-to-noise comparison in head images”. *Magn Reson Med* 2001;46(1):24-30.
6. Hoult DI, Phil D. Sensitivity and power deposition in a high-field imaging experiment. *J Magn Reson Imaging.* 2000;12(1):46-67.
7. Moser E, Stahlberg F, Ladd ME, Trattnig S. 7-T MR—from research to clinical applications? *NMR Biomed.* 2012;25(5):695-716.
8. Webb AG, Van de Moortele PF. “The technological future of 7 T MRI hardware”. *NMR Biomed* 2016;29:1305-15.
9. Wu X, Vaughan JT, Ugurbil K, Van de Moortele P-F. “Parallel excitation in the human brain at 9.4 T counteracting k-space errors with RF pulse design”. *Magn Reson Med* 2010;63(2):524-9.
10. Budde J, Shajan G, Zaitsev M, Scheffler K, Pohmann R. Functional MRI in human subjects with gradient-echo and spin-echo EPI at 9.4 T. *Magn Reson Med.* 2014;71(1):209-18.
11. Wu X, Adriany G, Ugurbil K, Van de Moortele PF. “Parallel transmission in human brain at 9.4T counteracting eddy current induced excitation errors in RF pulse design”. *Proc Intl Soc Mag Reson Med.* 2011;19:4441.
12. Budde J, Shajan G, Hoffmann J, Ugurbil K, Pohmann R. Human imaging at 9.4 T using T(2)\*-, phase-, and susceptibility-weighted contrast. *Magn Reson Med.* 2011;65(2):544-50.
13. Kangarlou A, Baertlein BA, Lee R, et al. Dielectric resonance phenomena in ultra high field MRI. *J Comput Assist Tomogr.* 1999;23(6):821-31.
14. Bomsdorf H, Helzel T, Kunz D, Roschmann P, Tschendel O, Wieland J. Spectroscopy and imaging with a 4 tesla whole-body MR system. *NMR Biomed.* 1988;1(3):151-8.
15. Barfuss H, Fischer H, Hentschel D, Ladebeck R, Vetter J. Whole-body MR imaging and spectroscopy with a 4-T system. *Radiology.* 1988;169(3):811-6.

16. Collins CM, Li S, Smith MB. "SAR and B1 field distributions in a heterogeneous human head model within a birdcage coil" Specific energy absorption rate. *Magn Reson Med* 1998;40(6):847-56.
17. Collins CM, Smith MB. Signal-to-noise ratio and absorbed power as functions of main magnetic field strength, and definition of "90 degrees" RF pulse for the head in the birdcage coil. *Magn Reson Med*. 2001;45(4):684-91.
18. Hoult DI. The principle of reciprocity in signal strength calculations - A mathematical guide. *Concepts in Magnetic Resonance*. 2000;12(4):173-87.
19. Hayes CE, Edelstein WA, Schenck JF, Mueller OM, Eash M. An efficient, highly homogeneous radiofrequency coil for whole-body NMR imaging at 1.5-T. *J Magn Reson*. 1985;63(3):622-8.
20. Vaughan JT, Snyder CJ, DelaBarre LJ, et al. Whole-body imaging at 7T: preliminary results. *Magn Reson Med*. 2009;61(1):244-8.
21. Alsop DC, Connick TJ, Mizsei G. A spiral volume coil for improved RF field homogeneity at high static magnetic field strength. *Magn Reson Med*. 1998;40(1):49-54.
22. Adriany G, Van de Moortele PF, Wiesinger F, et al. "Transmit and receive transmission line arrays for 7 Tesla parallel imaging". *Magn Reson Med* 2005;53(2):434-45.
23. Roemer PB, Edelstein WA, Hayes CE, Souza SP, Mueller OM. The NMR phased array. *Magn Reson Med*. 1990;16:192-225.
24. Katscher U, Bornert P, Leussler C, van den Brink JS. Transmit SENSE. *Magn Reson Med*. 2003;49(1):144-50.
25. Zhu Y. Parallel excitation with an array of transmit coils. *Magn Reson Med*. 2004;51(4):775-84.
26. Setsompop K, Wald LL, Alagappan V, et al. Parallel RF transmission with eight channels at 3 Tesla. *Magn Reson Med*. 2006;56(5):1163-71. PubMed PMID: 17036289.
27. Hetherington HP, Avdievich NI, Kuznetsov AM, Pan JW. RF shimming for spectroscopic localization in the human brain at 7 T. *Magn Reson Med*. 2010;63(1):9-19.
28. Setsompop K, Alagappan V, Gagoski B, et al. Slice-selective RF pulses for in vivo B1 + inhomogeneity mitigation at 7 tesla using parallel RF excitation with a 16-element coil. *Magn Reson Med*. 2008;60(6):1422-32.
29. Metzger GJ, Snyder C, Akgun C, Vaughan T, Ugurbil K, Van de Moortele PF. "Local B1 + shimming for prostate imaging with transceiver arrays at 7T based on subject-dependent transmit phase measurements". *Magn Reson Med* 2008;59(2):396-409.
30. Van de Moortele PF, Akgun C, Adriany G, et al. B-1 destructive interferences and spatial phase patterns at 7 T with a head transceiver array coil. *Magn Reson Med*. 2005;54(6):1503-18.
31. Brunner DO, De Zanche N, Frohlich J, Paska J, Pruessmann KP. Travelling-wave nuclear magnetic resonance. *Nature*. 2009;457(7232):994-8.
32. Brunner DO, Paska J, Froehlich J, Pruessmann KP. "Traveling-wave RF shimming and parallel MRI". *Magn Reson Med* 2011;66(1):290-300.
33. Zhang B, Wiggins G, Duan Q, Sodickson DK. "Design of a patch antenna for creating traveling waves at 7 tesla". In: *Proc of the 17th Scientific Meeting, International Society for Magnetic Resonance in Medicine*. Honolulu, HI, USA; 2009:4746.
34. Schmidt R, Webb A. *Improving travelling wave efficiency at 7 T using dielectric material placed "beyond" the region of interest*. Singapore: International Society for Magnetic Resonance in Medicine; 2016:3532.
35. Yan X, Zhang X, Gore JC, Grissom WA. Improved traveling-wave efficiency in 7T human MRI using passive local loop and dipole arrays. *Magn Reson Imaging*. 2017;39:103-109.
36. Vaughan JT, DelaBarre L, Snyder C, et al. eds. "9.4T human imaging: preliminary results". *Proc Intl Soc Mag Reson Med*; 2006;56:1274-1282.
37. Metzger GJ, Van de Moortele PF, Akgun C, et al. Performance of external and internal coil configurations for prostate investigations at 7 T. *Magn Reson Med*. 2010;64(6):1625-39.
38. Metzger GJ, Auerbach EJ, Akgun C, et al. "Dynamically applied B1 + shimming solutions for non-contrast enhanced renal angiography at 7.0 Tesla". *Magn Reson Med* 2013;69(1):114-26.
39. Raaijmakers AJE, Luijten PR, Van den Berg CA. "Dipole antennas for ultrahigh-field body imaging: a comparison with loop coils". *NMR Biomed* 2016;29:1122-30.
40. Djordjevic AR, Zajic AG, Ilic MM, Stuber GL. Optimization of helical antennas. *IEEE Antennas Propagat Magazine*. 2006;48(6):107-15.
41. Lee DJ, Glover PM, eds. "A Comparison of a Patch Antenna to an End-fire Helix Antenna for use in Travelling Wave MRI". Proc of the Joint Annual Meeting ISMRM-ESMRMB 2010; 2010; Stockholm.
42. Raaijmakers AJE, Van der Werf A, Kroeze H, Luijten PR, Van den Berg CAT, Klomp DWJ. "Helix antennas: approaching the target from a different angle". Proc of the Joint Annual Meeting ISMRM-ESMRMB 2014, Milan, Italy. 2014.
43. Notaros BM, Ilic MM, Tonyushkin AA, Sekeljic NJ, Athalye P. "Quadrifilar Helical Antenna as a Whole-Body Traveling-Wave RF Coil for 3T and 7T MRI". (Abstract) Proceedings of the 23th Scientific Meeting of the International Society for Magnetic Resonance in Medicine, ISMRM 2015, 30 May - 5 June, 2015, Toronto, Ontario, Canada. p.1825. 2015.
44. Ilic MM, Tonyushkin AA, Sekeljic NJ, Athalye P, Notaros BM. "RF excitation in 7 T MRI systems using monofilar axial-mode helical antenna". (APS Summary) Proc. of the 2015 IEEE International Symposium on Antennas and Propagation, July 19-25 2015, Vancouver, BC, Canada, pp. 1346-1347. 2015.
45. Athalye PS, Šekeljic NJ, Ilic MM, et al. "Long and Short Monofilar and Quadrifilar Helical Antenna RF Coils at 7 T". (Abstract) Invited Presentation. 10th Biennial 2015 Minnesota Workshop on High and Ultra-High Field Imaging, October 1-3, 2015, Minneapolis, MN. 2015.
46. Athalye PS, Ilic MM, Van de Moortele P-F, Kiruluta AJM, Notarosh BM. "Multi-Channel Helical-Antenna Inner-Volume RF Coils for Ultra-High-Field MR Scanners". (Abstract) Proceedings of the 24th Scientific Meeting of the International Society for Magnetic Resonance in Medicine, ISMRM 2016, 7-13 May 2016, Singapore. 2016.
47. Athalye PS, Šekeljic NJ, Ilic MM, Tonyushkin AA, Notarosh BM. Subject-loaded quadrifilar helical-antenna RF coil with high B1 + field uniformity and large FOV for 3-T MRI. *Concepts in Magnetic Resonance*. 2016;46B(3):106-17.
48. Kraus DJ. Helical beam antennas. *Electronics*. 1947;20:109-11.
49. Kraus DJ. *Antennas*. New York: McGraw-Hill; 1988.
50. Notaros BM. *Electromagnetics*. New Jersey: PEARSON Prentice Hall; 2010.
51. Djordjevic M, Notaros BM. Double higher order method of moments for surface integral equation modeling of metallic and dielectric antennas and scatterers. *IEEE Trans Antennas Propag*. 2004;52(8):2118-29.

52. Notaros BM. Higher order frequency-domain computational electromagnetics. *IEEE Trans Antennas Propag.* 2008;56(8):2251-76.
53. WIPL-D Pro v11. WIPL-D d.o.o. ed2014.
54. HFSS, ANSYS®. Electromagnetics Suite 15.0.7, ed: ANSYS, Inc.
55. Zhang B, Sodickson DK, Lattanzi R, Duan Q, Stoeckel B, Wiggins GC. Whole body traveling wave magnetic resonance imaging at high field strength: homogeneity, efficiency, and energy deposition as compared with traditional excitation mechanisms. *Magn Reson Med.* 2012;67:1183-1193.
56. Andreychenko A, Kroeze H, Klomp DWJ, Lagendijk JJW, Luijten PR, Van den Berg CAT. Coaxial waveguide for travelling wave MRI at ultrahigh field. *Magn Reson Med.* 2013;70:875-884.
57. Andreychenko A, Kroeze H, Boer VO, Lagendijk JJW, Luijten PR, Van den Berg CAT. Improved steering of the RF field of travelling wave MR with a multimode, coaxial waveguide. *Magn Reson Med.* 2014;71:1641-1649.
58. Sohn S-M, BelaBarre L, Anand G, Vaughan JT. RF head coil design with improved RF magnetic near-fields uniformity for magnetic resonance imaging (MRI) systems. *Magn Reson Med.* 2014;71:1641-1649.

**How to cite this article:** Athalye PS, Ilić MM, van de Moortele P-F, Kiruluta AJM, Notaroš BM. Multi-channel helical-antenna inner-volume RF coils for ultra-high field MR scanners. *Concepts Magn Reson Part B.* 2018;48B:e21405.  
<https://doi.org/10.1002/cmr.b.21405>